

# Journal of Biomedical Optics

BiomedicalOptics.SPIEDigitalLibrary.org

## **5-aminolevulinic acid induced protoporphyrin IX as a fluorescence marker for quantitative image analysis of high-grade dysplasia in Barrett's esophagus cellular models**

Shu-Chi Allison Yeh  
Samir Sahli  
David W. Andrews  
Michael S. Patterson  
David Armstrong  
John Provias  
Qiyin Fang

**SPIE.**

# 5-aminolevulinic acid induced protoporphyrin IX as a fluorescence marker for quantitative image analysis of high-grade dysplasia in Barrett's esophagus cellular models

Shu-Chi Allison Yeh,<sup>a</sup> Samir Sahli,<sup>b</sup> David W. Andrews,<sup>c</sup> Michael S. Patterson,<sup>d</sup> David Armstrong,<sup>e</sup> John Provias,<sup>f</sup> and Qiyin Fang<sup>a,b,\*</sup>

<sup>a</sup>McMaster University, School of Biomedical Engineering, 1280 Main Street West, Hamilton, Ontario L8S 4K1, Canada

<sup>b</sup>McMaster University, Department of Engineering Physics, 1280 Main Street West, Hamilton, Ontario L8S 4K1, Canada

<sup>c</sup>Sunnybrook Research Institute, 2075 Bayview Avenue, Toronto, Ontario M4N 3M5, Canada

<sup>d</sup>McMaster University, Department of Medical Physics and Applied Radiation Sciences, 1280 Main Street West, Hamilton, Ontario L8S 4K1, Canada

<sup>e</sup>McMaster University, Department of Medicine, Division of Gastroenterology, 1280 Main Street West, Hamilton, Ontario L8S 4K1, Canada

<sup>f</sup>McMaster University, Department of Pathology and Molecular Medicine, Division of Neuropathology, 1280 Main Street West, Hamilton, Ontario L8S 4K1, Canada

**Abstract.** Early detection and treatment of high-grade dysplasia (HGD) in Barrett's esophagus may reduce the risk of developing esophageal adenocarcinoma. Confocal endomicroscopy (CLE) has shown advantages over routine white-light endoscopic surveillance with biopsy for histological examination; however, CLE is compromised by insufficient contrast and by intra- and interobserver variation. An FDA-approved PDT photosensitizer was used here to reveal morphological and textural features similar to those found in histological analysis. Support vector machines were trained using the aforementioned features to obtain an automatic and robust detection of HGD. Our results showed 95% sensitivity and 87% specificity using the optimal feature combination and demonstrated the potential for extension to a three-dimensional cell model. © 2015 Society of Photo-Optical Instrumentation Engineers (SPIE) [DOI: 10.1117/1.JBO.20.3.036010]

Keywords: Barrett's esophagus; feature extraction; support vector machines; 5-aminolevulinic acid; endomicroscopy.  
Paper 140686RR received Oct. 18, 2014; accepted for publication Feb. 23, 2015; published online Mar. 19, 2015.

## 1 Introduction

Esophageal adenocarcinoma (EAC) is a malignant cancer with a low five-year survival rate of 12% due to the lack of early diagnosis.<sup>1-3</sup> EAC is associated with high-grade dysplasia (HGD) in a setting of Barrett's esophagus (BE), a premalignant condition in which the normal squamous epithelium is replaced by intestinal metaplasia that may eventually progress via low-grade dysplasia to HGD.<sup>4</sup> Although endoscopic surveillance is performed regularly on patients with BE in an attempt to achieve early diagnosis, substantial sampling and relocation errors still exist due to the nature of the random four-quadrant biopsy protocol and temporal separation of the diagnostic and treatment procedures.<sup>5</sup> Therefore, integrated real-time diagnosis and treatment (seek-and-treat) is an ideal strategy to overcome these challenges. Optical biopsy is an emerging technique that probes the optical properties of targeted lesions during the examination, with the potential for achieving real-time diagnosis.<sup>3,6</sup> However, there are still major challenges when investigating BE. In general, the diagnostic accuracy of point spectroscopy is strongly affected by patient-to-patient variability.<sup>5</sup> Also, insufficient sensitivity and specificity are found particularly in autofluorescence BE imaging due to poor signal-to-noise ratio.<sup>7</sup> To overcome these limitations, *in vivo* histology using confocal endomicroscopy (CLE) and a suitable exogenous contrast agent holds advantages in showing real-time cytological information of clinical histology standards: HGD cells are

characterized by cytological features of atypia, including, particularly, nuclear pleomorphism as well as loss of cell polarity, crowded nucleus distribution, overlapping of cell borders, enlarged nucleus-to-cytoplasm ratio, and nuclear stratification. In contrast, intestinal metaplasia demonstrates well-spaced, rounder, and more basally oriented nuclei. Gross observation shows the nondistorted architecture, existence of goblet cells, and less stratified morphology.<sup>8,9</sup>

In recent years, machine learning has emerged as a potential technique to automate the detection of premalignant lesions and prevent inter- and intraobserver variability.<sup>10,11</sup> Muldoon et al. used high-resolution microendoscopy and a nucleus contrast agent, proflavin, to perform automatic imaging recognition of neoplastic lesions and obtained sensitivity and specificity of 0.87 and 0.85, respectively.<sup>10</sup> Although these cellular resolution technologies have been extensively investigated and have demonstrated desirable sensitivity and specificity, the use of a contrast agent capable of highlighting HGD remains controversial. For example, nucleus stains exhibit better cytological patterns by which to identify HGD,<sup>9</sup> but are considered mutagenic. Other commercial dyes are relatively safer but yield poor selectivity for HGD.<sup>12</sup> Common markers for the GI tract and their properties are summarized in Table 1; unfortunately, most do not provide sufficient contrast to allow an accurate identification of HGD.<sup>5,10,12-18</sup>

\*Address all correspondence to: Qiyin Fang, E-mail: [qiyin.fang@mcmaster.ca](mailto:qiyin.fang@mcmaster.ca)

**Table 1** Common contrast agents in esophageal chromoendoscopy.

Contrast agents	Properties and applications
Fluorescein	Highlights vasculature and intracellular space; goblet cells and epithelial mucin appear dark <sup>12,13</sup>
Methylene blue	Highlights actively absorbing columnar epithelium but with little discrimination for high-grade dysplasia (HGD) <sup>16,17</sup>
Toluidine blue	Stains nuclei of columnar cells <sup>17</sup>
Lugol's solution	Stains only normal mucosa for its affinity to iodinated agents <sup>14</sup>
Cresyl violet	Stains the cytoplasm and highlights cell nuclei; the staining pattern does not provide adequate discrimination <sup>15,18</sup>
Acriflavin	Stains cell nuclei directly, but is considered to be mutagenic <sup>10</sup>
Acetic acid	Highlights columnar mucosa, but low specificity for HGD <sup>5</sup>
Indocyanine green	Less used in chromoendoscopy; mainly used for marking locations <sup>17</sup>

As a result, FDA-approved photodynamic therapy (PDT) photosensitizers that cause fluorescence of mitochondria become attractive alternatives to “nucleus” contrast agents, and the fluorescence lifetime of photosensitizers may provide additional contrast for probing cellular uptake.<sup>19</sup> More importantly, PDT photosensitizers also offer potential treatment selectivity.<sup>20,21</sup> To study this seek-and-treat strategy, we started with a well-characterized *in vitro* BE model<sup>22</sup> that demonstrated cell line competition in two-dimensional (2-D) and three-dimensional (3-D) coculture<sup>23,24</sup> with close cytogenetic similarities to BE *in vivo*<sup>22,25</sup> and less experimental variability than animal models.<sup>24,26</sup> The eventual goal of this study is to translate knowledge gained from this coculture platform to HGD detection using clinically available CLE.<sup>18</sup> In a pilot study using 5-aminolevulinic acid (5-ALA) induced protoporphyrin IX (PpIX) as a contrast agent, we began with morphological and textural features at a single-cell level in monoculture. Generalization of the training algorithm was further evaluated in coculture, which could be further extended to be compatible with histology standards<sup>9</sup> using high-density cell culture.

## 2 Materials and Methods

We studied 5-ALA induced PpIX synthesis in both metaplasia and HGD cell lines to investigate its potential as a contrast agent to highlight cellular morphology in CLE. Image analysis was performed to extract morphological and texture features based on PpIX fluorescence, and support vector machines (SVM) were trained to classify cocultured cells. The classification performance of the SVM was then characterized.

### 2.1 Monoculture and Coculture

CP-A (non-dysplastic metaplasia, ATCC® CRL-4027™) and CP-B (high-grade dysplasia, ATCC® CRL-4028™) are hTERT immortalized human Barrett's esophageal cell lines.<sup>22–24</sup> In

order to provide the ground truth for the classification results in coculture, parental CP-A cells were further transfected with a cytosolic mCerulean3 construct to achieve cyan fluorescence, which offers the advantage of not overlapping with the PpIX spectrum. The stably transfected CP-A cells were expanded using the complete culture medium containing 5  $\mu\text{g}/\text{ml}$  selective antibiotics (Blasticidin S HCl, R210-01, Gibco®, Canada). As some nonfluorescent cells may develop resistance to the selective antibiotics, a flow cytometer (FACSCanto™, BD Biosciences, California) was used to further purify mCerulean3 expressing cells. Stable cells were then maintained using complete medium supplemented with 3  $\mu\text{g}/\text{ml}$  of Blasticidin S.

The complete medium used for all cell lines was composed of MCDB 153 base medium (M7403, Sigma), supplemented with 5% fetal bovine serum (16000-036, Gibco®), 0.25  $\mu\text{g}/\text{ml}$  amphotericin B (A2942, Sigma), 1% penicillin/streptomycin (15140-122, Gibco®), 0.4  $\mu\text{g}/\text{ml}$  hydrocortisone (H0888, Sigma), 140  $\mu\text{g}/\text{ml}$  bovine pituitary extract (P1476, Sigma), 20 mg/l adenine (A8626, Sigma), 0.1% insulin-transferrin-sodium selenite (I1884, Sigma), 20 ng/ml recombinant EGF (E9644, Sigma), 4 mM glutamine, and 1 nM cholera toxin (C8052, Sigma). Cells were grown in 25 cm<sup>2</sup> culture flasks and maintained at 37°C in a water jacketed CO<sub>2</sub> incubator (Forma Series II, Thermo Fisher Scientific Inc., Waltham, Massachusetts). The subculturing procedures followed the recommendation from ATCC, where cells were immersed in 1 ml trypsin-EDTA solution (2.5X, 0.5%, 15400-054, Gibco®) until fully detached and neutralized by complete culture medium followed by centrifugation at 125 g in order to resuspend cells in fresh trypsin-free culture medium.

### 2.2 Sample Preparation

A 100 mM stock solution of 5-ALA (A3785, Sigma) dissolved in phosphate buffered saline (14190-144, Gibco®) was stored in aliquots in the dark. A working concentration of 0.5 mM was prepared before every experiment by further diluting the stock solution in the serum-free complete culture medium. Cells were seeded on glass-bottom dishes (P35G-1.5-14-C, MatTek, Massachusetts) one day before the experiment. Before imaging acquisition, individual cell lines were incubated with 5-ALA for various periods of time between 3 and 6 h to yield different mitochondrial PpIX concentrations for training of the classification algorithm. This variable was intentionally introduced to characterize intracellular PpIX concentration and account for variability in fluorescence intensity during classification. Coculture preparation used a total of  $0.3 \times 10^5$  cells containing mCerulean3-CP-A and parental CP-B in 1 : 1 ratio with the incubation of 5-ALA for 6 h.

### 2.3 Imaging Acquisition

The fluorescence emission of 5-ALA induced PpIX was collected between 625 and 750 nm by a laser scanning confocal microscope (TCS SP5 & DMI 6000 B, Leica, Wetzlar, Germany) equipped with an argon-ion laser operating at 514 nm. The emission spectral band starting from 625 nm was used to maximize the detected PpIX intensity while avoiding overlap with the mCerulean3 spectrum. A 63 $\times$  objective lens was used to yield a field of view of 246  $\mu\text{m} \times 246 \mu\text{m}$  with lateral resolution of  $\sim 300$  nm, comparable to current confocal endomicroscopy systems.<sup>12</sup> The acquisition channel for transfected CP-A cells in coculture used 458 nm laser excitation

with the emission spectral range of 465 to 500 nm to match the fluorescence emission peak of mCerulean3. Sample fluorescence images of both cell lines in monoculture and coculture are demonstrated in Figs. 1 and 2.

## 2.4 Quantifying Intracellular PpIX in Mono- and Coculture

To investigate the feasibility of using PpIX as a contrast agent, the cellular uptake was compared for metaplastic and HGD cells. Both cell lines were incubated with 5-ALA solution for a specified time and fluorescence images were acquired every hour using both one-photon (5.92 J/cm<sup>2</sup>) and two-photon excitation (9911 J/cm<sup>2</sup>) until the intracellular PpIX reached a plateau. PpIX intensities in coculture were compared only at 6 h of incubation. All acquisition parameters, including the fluence, magnification, emission spectral range, and the detector gain remained the same in repetitive trials using different batches of cells. The acquired images were preprocessed with consistent procedures to segment the fluorescent area using MATLAB® (MathWorks, Natick, Massachusetts). The average PpIX intensity per pixel was then plotted against the incubation period.

## 2.5 Segmentation and Feature Extraction

The images were imported to MATLAB® for further image processing and feature extraction. Due to the low signal-to-noise ratio provided by PpIX, all fluorescence images were preprocessed to reduce the shot noise and uneven background. Contrast was enhanced by three iterative adjustments of imaging threshold, followed by further smoothing and morphological operations to produce segmented binary images of each cell. The segmentation results are demonstrated in Fig. 3. Then, mitochondrial distribution was analyzed using various morphological features based on the binary images to illustrate the shape eccentricity, irregularity, and the nucleus-to-mitochondria ratio.<sup>9,27</sup> Textural features, such as PpIX fluorescence patterns, of each cell were explored using calculation of the intensity histogram.<sup>27</sup> Further textural analysis was achieved using the gray-level co-occurrence matrix (GLCM)<sup>28</sup> along perpendicular

and diagonal axes of the bounding box to extract intensity contrast, correlation, homogeneity, and energy. Note that the textural features were extracted from 8-bit intensity images. The key features and their descriptions are summarized in Table 2.

## 2.6 Feature Reduction and Classification

An image dataset containing a total of 62 CP-B and 63 CP-A cells from monoculture were used to train the SVM. Morphological and textural features extracted from each individual cell are concatenated to form a 15-dimensional feature vector which characterizes the cells. Most of the features contain redundant information and are highly correlated. Therefore, reduction of feature dimensionality was first performed using a forward sequential selection (FSS) algorithm (*sequentialfs*, MATLAB®, MathWorks).<sup>29</sup> In the feature selection process, individual features were sequentially recruited and tested for their prediction accuracy using linear discriminant analysis with 10-fold cross-validation.<sup>30</sup> This operation splits the whole training set into 10 subgroups, followed by iterative classification on every single subgroup using the training algorithm obtained from the other nine-tenths of the datasets. This feature reduction step renders a combination of feature subsets that yields the smallest misclassification error [as shown in Fig. 5(a)].

Using the best feature subsets returned from the FSS algorithm, SVM were then trained to classify each cell in the coculture to CP-A (metaplasia) or CP-B (HGD). SVM mapped the input features to a higher-dimensional space to find the hyperplane that yields the largest margin between the two classes. The Gaussian radial basis function (RBF) kernel was applied to deal with potential nonlinear relationships between the feature attributes and the class, thus yielding a soft margin.<sup>31</sup> Given the training sets, the RBF kernel radius ( $R$ ) and the box constraint ( $C$ ) were optimized using fivefold cross-validation. A total of 109 CP-A and 135 CP-B cells in coculture were then used for testing the classification performance. The performance of the SVM was measured by sensitivity and specificity. The sensitivity is defined as the ratio of correct HGD detection to true CP-B numbers, and the specificity corresponds to the ratio of correct

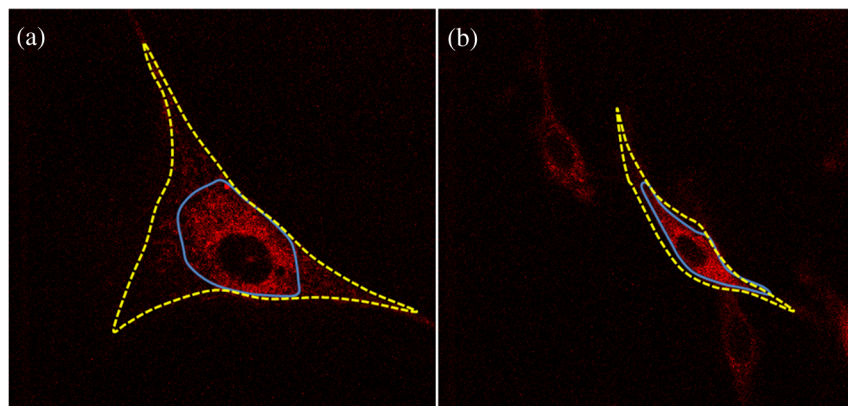


**Fig. 1** Sample CP-A and CP-B cells labeled with fluorescent protoporphyrin IX (PpIX) in monoculture conditions. Cells were loaded with 5-aminolevulinic acid (5-ALA) and the PpIX fluorescence was examined within 6 h of incubation. The fluorescent area (mitochondria distribution) is highlighted by the solid line, and the cell shapes based on the bright-field images are indicated by the dashed line. PpIX fluorescence yielded distinct morphological and textural patterns in (a) CP-A cells and (b) CP-B cells. CP-A cells yielded a more concentrated fluorescence accumulation toward the perinuclear region, while CP-B cells demonstrated a more elongated shape. Further image processing and segmentation was performed for classification of CP-B cells.

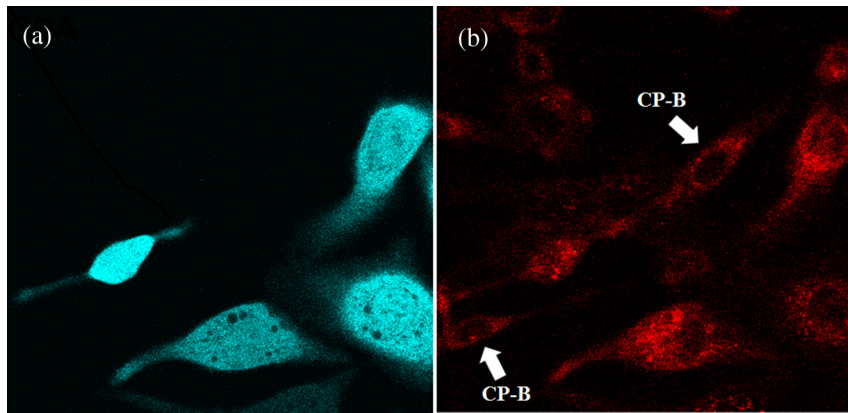


**Fig. 2** Stably transfected CP-A cells were used for validation of the classification results. In the same region of co-culture shown in (a) and (b), (a) the CP-A cells expressing mCerulean3 are identified from the emission band of 465 to 500 nm, (b) thus serving as ground truth when both CP-A and CP-B (white arrows) are stained with 5-ALA induced PpIX.

metaplasia detection to true CP-A numbers. Performance of the classification algorithm was further assessed by plotting the receiver operating characteristic (ROC) curve and calculating the area under the curve (AUC), as shown in Figs. 5–8.

### 3 Results

#### 3.1 Evaluation of Time-Lapse PpIX Fluorescence Intensity

To evaluate the use of 5-ALA for detection of dysplastic cells, we first characterized the cellular uptake of the two cell lines in monoculture. The intracellular PpIX intensities were plotted against the incubation time as shown in Figs. 4(a) and 4(b). The results showed that CP-B cells reached maximum PpIX concentration faster (within 3 h) than CP-A cells, where the PpIX intensities at 3 h were  $32 \pm 3$  counts in CP-B and  $23 \pm 2$  counts in CP-A using one-photon excitation ( $p < 0.01$ ). The data acquired using two-photon excitation demonstrated a similar trend. In addition, it was clearly shown that there was no selective accumulation of PpIX in HGD cells with neoplastic characteristics; instead, both cell lines exhibited similar

saturation intensities after 5 h of 5-ALA incubation. As shown in Fig. 4(c), the lack of cellular uptake selectivity ( $p = 0.51$ ) was also observed in a coculture environment, where the PpIX intensities in both cell lines agreed with the monoculture results. Although we are comparing metaplasia versus HGD, the results are consistent with a previous study showing that BE tissue exhibited a faster PpIX accumulation within 4 h compared to normal epithelium, and the eventual maximum intensity was higher in normal epithelium.<sup>32</sup> The conversion and saturation intensity of PpIX may depend on the activity and amount of ferrochelatase.<sup>21,32</sup>

#### 3.2 Reduction of Dimensionality

The rank of features in the recruiting process using the FSS algorithm is indicated by the superscripts in Table 2. A lower value indicates a higher prevalence of the given feature. The examination of feature combination is then based on this sequence. During sequential feature recruiting performed with the monoculture training group, combinations of a range of feature numbers were examined for their classification performance.

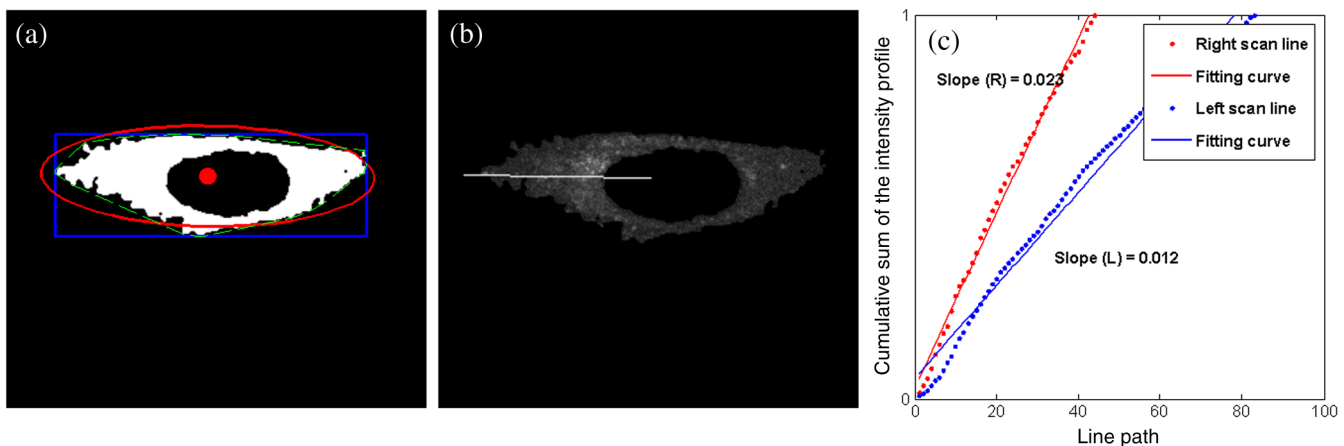


**Fig. 3** Examples of morphological and textural features. (a) A binary image is used to extract morphological features. The bounding box, convex area (area within dashed lines), and the ellipse are noted. (b) The original 8-bit image of mitochondria distribution was obtained using the binary mask. This image shows the line used for extracting the line scan intensity profile as described in Table 2. (c) The intensity contrast can be represented by the slope of the cumulative intensity along the line. The slope (L) is from the line shown in Fig. 3(b), and the slope (R) is obtained from the line in the opposite direction.

**Table 2** List of features

Morphological features	Descriptions
Eccentricity of the ellipse <sup>a</sup>	Ratio of the distance between the two foci to the length of the major axis of the ellipse; larger values indicate slender shapes
Major to minor axis ratio <sup>e</sup>	Ratio of the lengths of the two axes of the ellipse; larger values indicate slender shapes
Extent <sup>g</sup>	Binary pixel area divided by the bounding box area; slender cells with various orientations lead to smaller values
Solidity <sup>f</sup>	Binary pixel area divided by the convex area [indicated in Fig. 3(a)] to demonstrate shape irregularity
Roundness	$(4\pi \times \text{Area})/(\text{Perimeter}^2)$ ; the value of 1 indicates a perfect circle
Nucleus to mitochondria ratio <sup>c</sup>	Ratio of the binary pixel area of the segmented cell nucleus to the area of the mitochondria identified by protoporphyrin IX
Intensity/textural features	Descriptions
Line scan intensity profile <sup>b</sup>	Cumulative intensity profile along the line from the centroid to one end of the ellipse; a single value of slope was obtained to represent the profile
Standard deviation <sup>h</sup>	Standard deviation of the pixel intensity in the segmented region shown in Fig. 3(b)
Smoothness <sup>j</sup>	$1 - 1/(1 + \sigma^2)$ , where $\sigma$ represents variance of the intensity histogram
Third moment <sup>i</sup>	Indicates the symmetry of the intensity histogram of the segmented region
Entropy	Randomness of intensity values within the segmented region
GLCM contrast <sup>b</sup>	Contrast of pixel intensity to adjacent pixels over the segmented area
GLCM correlation	Correlation of neighbor pixel intensity over the segmented regions
GLCM homogeneity	Higher homogeneity is given when GLCM elements concentrate along the diagonal
GLCM Energy <sup>d</sup>	Sum of the squared elements of the matrix over the entire region

Note: GLCM, gray-level co-occurrence matrix.; Superscripts indicate the recruiting sequence of top 10 features during feature reduction, as described in Sec. 2.6.; \* showed comparable discriminant capability returned by sequential forward feature selection.

As shown in Fig. 5(a), the misclassification rates (MCR) were plotted against the number of features selected. The same combinations of features returned by feature selection were then tested in coculture classification. It is noted that the MCR converged to 0.10 when more than four features were used for the monoculture group, while only two features (eccentricity and line scan intensity profile) were required to produce the MCR to 0.09 when the same feature subsets were used in

coculture classification. With the reduced feature dimensionality, the performance of SVM for coculture classification was further demonstrated in Fig. 5(b), where ROC curves were plotted for various feature numbers. The best prediction performance using two features achieved an AUC of 0.95. There is a trend that the error of coculture classification is almost doubled after three features. This could be due to the fact that the other features are not as discriminating and that they add noise to the process. Extraction of features can be a time-consuming task since it requires computing geometric, intensity, and texture features from each cell. Obtaining such a high AUC with only two features selected via sequential feature recruiting is a promising result since the SVM can use these two identified features alone for classifying CP-A versus CP-B cells in the context of 2-D coculture. From a computational point of view, this result opens the way for online implementation of CP-A–CP-B classification.

### 3.3 Classification Performance Using Support Vector Machines

Without any specified stopping criterion, the feature selection process returned two subsets: one comprised eccentricity and the slope of the line scan intensity profile, and the other comprised eccentricity and GLCM contrast. Figures 6 and 7 demonstrate the training results using monoculture cells and the corresponding classification results on the cocultured cells. Figure 6 shows the training results based on eccentricity and GLCM contrast using the SVM with a Gaussian kernel. The two optimized parameters for the kernel,  $R$  (2.21) and  $C$  (1.07), account for the radius of the Gaussian kernel and the imbalance of the group population, respectively. Although the training result demonstrates sensitivity of 90% and specificity of just 74%, the combined classification results from all coculture images of repetitive trials showed 94% sensitivity and 82% specificity. The ROC curves that demonstrate the trade-off of sensitivity and specificity are shown in Fig. 8. Figure 7 shows the training results based on eccentricity and the slope obtained from the line scan profile. This training result was obtained with a sensitivity of 95% and specificity of 70% with  $R$  and  $C$  of 2.17 and 0.78, respectively; however, the classification produced an improved prediction on the coculture set, for which 95% sensitivity and 87% specificity were obtained with an AUC of 0.95 (Fig. 8). Table 3 summarizes the classification results from both monoculture and coculture, indicating a good generalization capability of the classifier from monoculture to coculture environment.

## 4 Discussion

We used a PDT photosensitizing agent, 5-ALA, to induce PpIX as a fluorescence marker to highlight mitochondria and generate nucleus contrast in Barrett's esophageal cell lines. Imaging contrast induced by PpIX is promising for its safety compared to regular nucleus stains, and its ability to delineate the nucleus in contrast to the highlighted mitochondria. Our results indicated that the HGD cells (CP-B) can be distinguished from metaplastic (CP-A) cells based on extracted features: their mitochondrial distribution (i.e., morphology revealed by PpIX fluorescence) and intensity patterns (i.e., line scan intensity profile), to reach an AUC of 0.95. Although the current study was based on an *in vitro* platform, the feasibility of using photosensitizers as contrast agents for automatic and robust detection of premalignant cells in coculture has been demonstrated. The

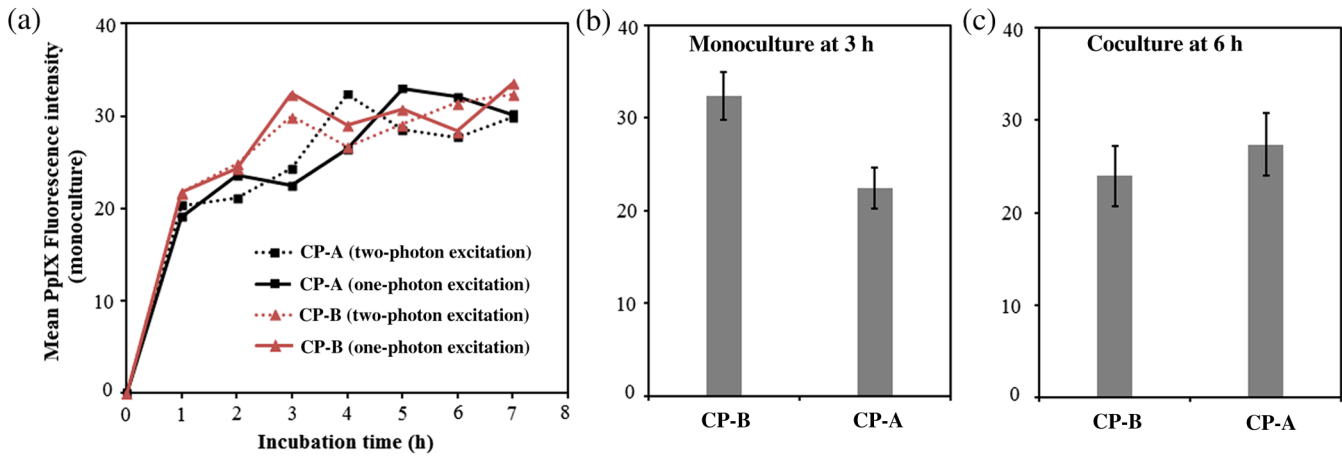


**Fig. 4** (a) The average intracellular PpIX intensity of each cell line in monoculture was plotted against the incubation time from 0 to 7 h using one-photon (solid line) and two-photon excitation (dotted line). It was noted that CP-B cells exhibit a higher PpIX intensity than CP-A at 3 h. The intracellular PpIX intensity eventually reached a plateau. The standard deviation of each data point was not shown in the figure for easy visualization. (b) PpIX intensity of CP-B and CP-A in monoculture measured at 3 h ( $p < 0.01$ ) using one-photon excitation. (c) Intracellular PpIX intensities were compared between the two cell lines grown in coculture environment after 6 h of 5-ALA incubation ( $p = 0.51$ ). The error bars represent the standard deviation of the mean.

quantitative image processing and classification yielded a better selectivity when compared with previous clinical studies based solely on 5-ALA preferential uptake,<sup>33</sup> where photobleaching was not an issue, but the confounding PpIX fluorescence found in nondysplastic regions led to a high rate of misclassification errors. The current study also provides promising results when compared with a previous imaging study using other contrast agents *in vivo*,<sup>10</sup> but an extension from the current study to a 3-D environment is necessary for a more direct comparison.

Because this is the first use of 5-ALA for automatic detection, we started logically by investigating the cellular uptake in monoculture and coculture. The intensity variation over time and the lack of selective uptake both motivated the development

of automatic and robust detection algorithms based on morphological and textural features. For example, in clinical applications, the inadequate detection accuracy may be attributed to lack of drug selectivity,<sup>34</sup> varied uptake rate, and artifacts from detection geometry.<sup>35</sup> In other words, training procedures that took the intensity variation into account might improve the classifier. Feature extraction and classification in this study were initially performed at the single-cell level in an attempt to have a thorough understanding of the morphological and cellular textural features that could potentially be retained in the next step that will conform to histological standards.<sup>9</sup> In order to establish a connection toward the 3-D model, we also acquired images of high density cell culture, where the cell-cell interaction is more

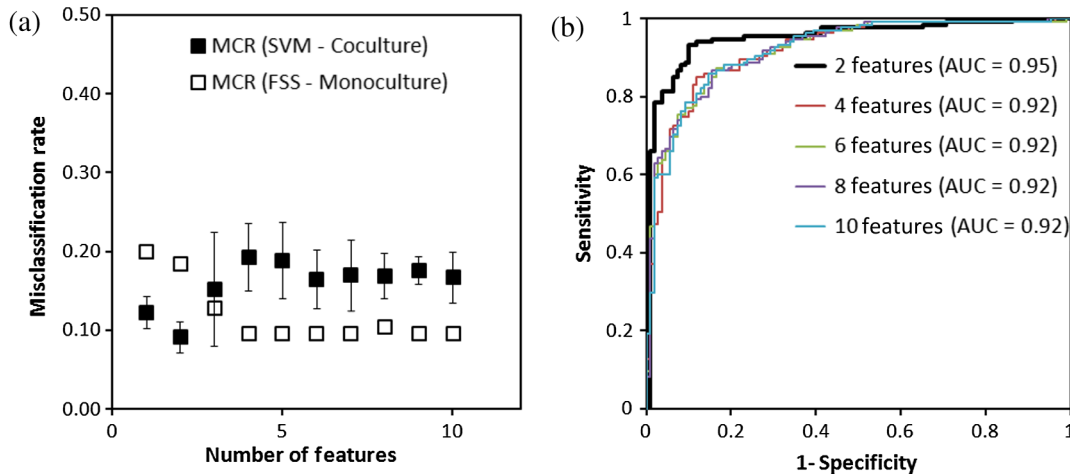


**Fig. 5** (a) Misclassification rates were plotted against up to 10 features used for classification. The results from the training set using monoculture yielded a misclassification rate (MCR) of 0.10 when four features were used. It is noted that classification results using the same feature subsets in coculture yielded an MCR of 0.09 when only the eccentricity and line scanned intensity profile were employed. The error bars represent standard deviation of coculture testing sets from three separate acquisition trials. (b) Receiver operating characteristic curves were obtained from support vector machine (SVM) classification on all coculture samples, and an area under the curve (AUC) of 0.95 can be achieved using the two features returned by feature selection, as indicated by the bold black line.

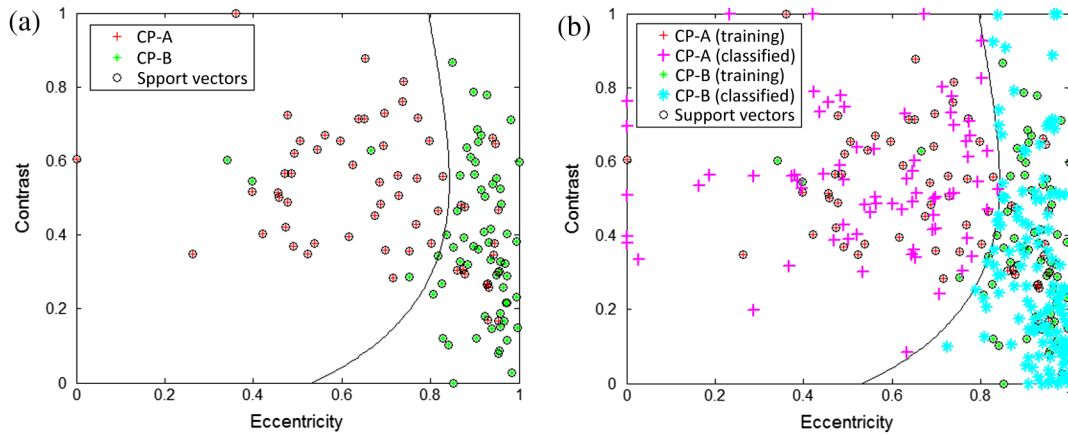


**Fig. 6** (a) The training results based on eccentricity and intensity contrast, which yield sensitivity of 90% (true CP-B) and specificity of 74% (true CP-A). (b) The trained model was tested on a combination of coculture imaging trials. The classification results demonstrated 94% sensitivity and 82% specificity.

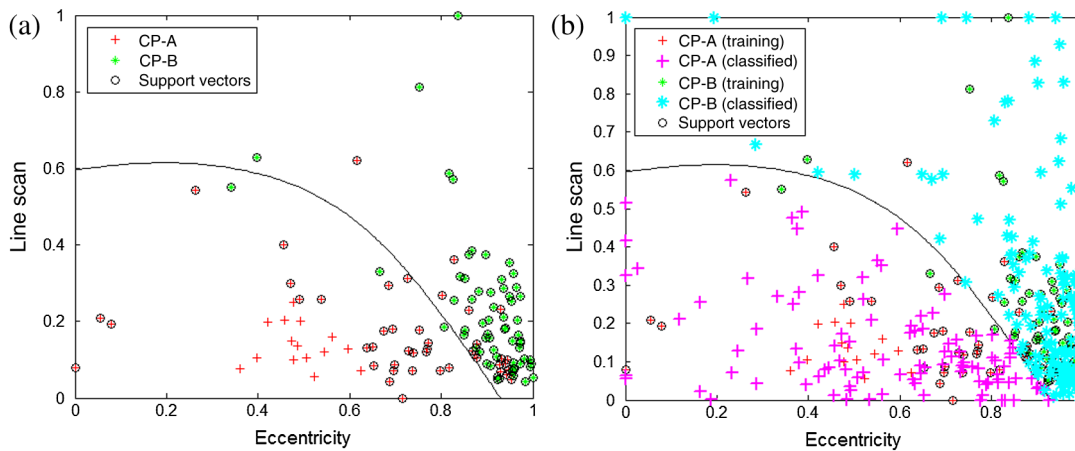


**Fig. 7** (a) The training results based on eccentricity and the slope obtained from the line scan profile using the same training set and testing set. This training showed sensitivity of 95% (true CP-B) and specificity of 70% (true CP-A). (b) The results from coculture images showed 95% sensitivity and 87% specificity.

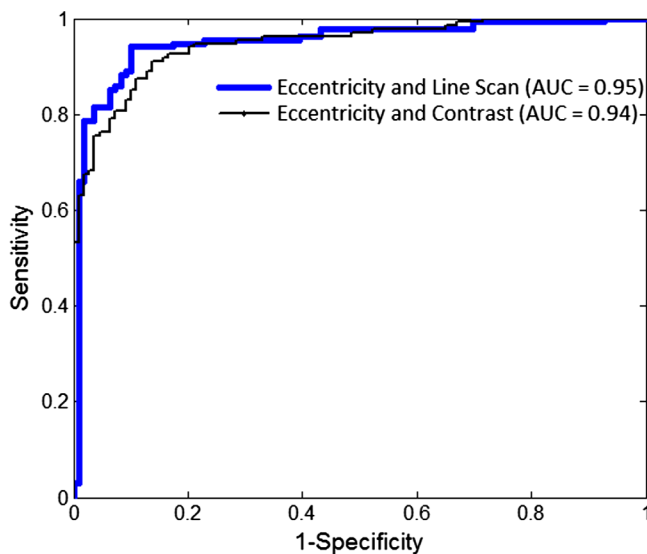


**Fig. 8** Performance of SVM using two features: the combination of eccentricity and intensity contrast (AUC = 0.94), and the combination of eccentricity and the slope obtained from the line scan intensity profiles (AUC = 0.95).

prominent and could yield distinct distribution patterns for classification. Figure 9 demonstrates high-density monoculture and coculture images stained with fluorescent PpIX. It is clear that the nucleus contrast highlighted by PpIX can yield features compatible with both single-cell analysis and histology guidelines. For example, the intrinsically greater eccentricity and more homogeneous intensity distribution of HGD cells were still observed in the high cell density environment [Fig. 9(b)]. These features are information hidden in the more randomly oriented nuclei and overlapped structure found in a region of HGD. More importantly, irregular nucleus size, orientation, and the formation of crowded and nonuniform stratified pattern were observed in CP-B [Fig. 9(b)] compared to CP-A cells [Fig. 9(a)], which is consistent with histological analyses.<sup>8,9</sup> This preliminary study, thus, provides baseline features for investigating high density and multilayered cell culture for identification of HGD regions as indicated in Fig. 9(c).

In this study, higher sensitivity and lower specificity were observed during the training process, but the specificity was increased during the classification using coculture datasets. From a drug uptake perspective, a maximum level of PpIX can be accumulated in mitochondria within 5 to 6 h. The higher the accumulation of PpIX in mitochondria, the better is the

**Table 3** Summary of the classification results.

Features	Groups	Sensitivity (%)	Specificity (%)
Eccentricity and contrast	Monoculture	90	74
	Coculture	94	82
Eccentricity and line scan	Monoculture	95	70
	Coculture	95	87

intensity contrast of the mitochondrial distribution. This phenomenon improves the classification of CP-A cells that exhibit greater intensity contrast compared to CP-B. It may be beneficial to further investigate the classification results on the testing coculture sets at various incubation times. Moreover, it is also observed that the use of fewer features can achieve better classification performance in coculture compared to monoculture, as shown in Fig. 5(a). This may be attributed to the fact that a coculture environment provides better control over experimental variability on both cell lines. Therefore, a comparable classification performance can be achieved using simpler feature combinations.

Relatively small numbers of cells were used to develop the classification algorithms. A larger sample population more likely represents population variability better. To address this

issue, monoculture and coculture images in this study were obtained from multiple independent experiments using different batches of cells growing in identical conditions with the same image acquisition settings. Individual cell lines from various batches were observed to have very similar morphology and drug uptake rate, suggesting a consistency in morphologic and fluorescence intensity patterns within each cell line. Furthermore, the use of stably transfected CP-A cells could also lead to the additional variability of CP-A cells. However, the transfection-associated changes in morphology and intensity texture can be validated by preliminary flow cytometry results: the forward scattering (size) and the side scattering (granularity) of transfected cells yielded a distribution pattern totally different from CP-B cells, but with the same distribution as CP-A cells (Fig. 10). In other words, the transfection did not alter cell morphology and granularity significantly. This can also be observed in Figs. 6 and 7, where the CP-A (training set) and transfected cells (in c-culture testing set) in the classification showed significantly overlapped distributions.

It should be noted that BE *in vivo* is a highly heterogeneous environment where different types of cells coexist. In this case, the discrimination would not only be between two cell lines, but several cell types. In clinical practice, the endoscopist takes biopsy samples based on visual observation of metaplasia, characterized by salmon pink color different from normal squamous epithelium. Within metaplasia tissue, the pathologist has to confirm the presence of HGD, as metaplasia and dysplasia are not

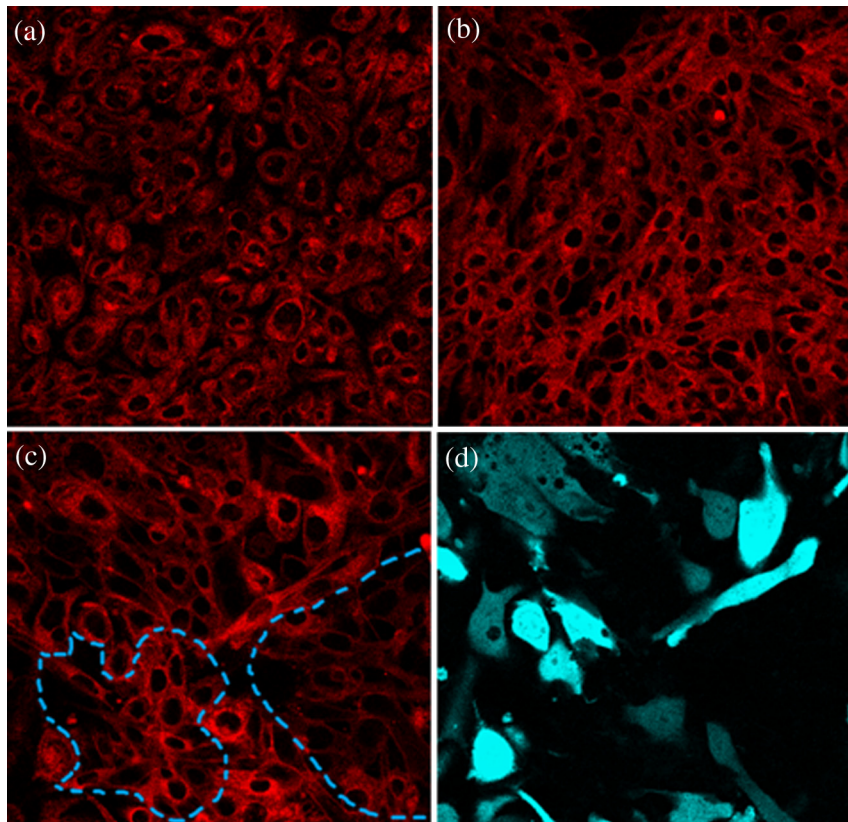


**Fig. 9** Sample images of high density monoculture and coculture cells incubated with 5-ALA for 6 h: (a) Monolayer CP-A (metaplasia) cells and (b) CP-B cells (high-grade dysplasia) that always form nodes of multiple layers before expanding. (c) Coculture image containing both CP-A and CP-B cells where certain CP-B areas are highlighted by the dashed line. (d) The same field of view as (c) where CP-A cells were stably transfected with mCerulean3 for the ground truth fluorescence channel.

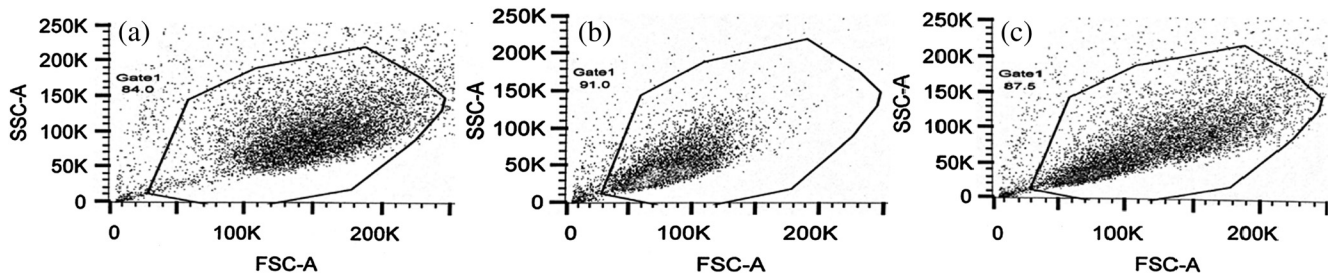


**Fig. 10** Cell size (forward scattering, FSC-A) and granularity (side scattering, SSC-A) demonstrated by the flow cytometry measurements: (a) parental CP-A cells, (b) parental CP-B cells, and (c) coculture of transfected CP-A and parental CP-B cells using 1:1 seeding ratio. The same gate was used to collect the cell count and the CP-A cells were also separated by the mCerulean emission. Both transfected and parental CP-A showed overlapping distributions in terms of size and granularity, in which the granularity is associated with the fluorescence intensity contrast in the cell. On the contrary, CP-B cells are of small cell size and less granularity than CP-A cells.

easily distinguished by wide-field observation. Therefore, we aim to distinguish these two very similar cell lines (metaplasia and HGD) as a starting point, which essentially could be a more challenging task compared to classification between normal and BE cells.

## 5 Conclusion

In conclusion, this preliminary study suggests that using a clinically approved photosensitizer as a contrast agent with the aid of machine learning may be a feasible approach for automatic and robust detection of HGD or premalignant cells. This approach overcomes the poor selectivity of clinical photosensitizers for BE, provides safer nucleus contrast for detection, and, potentially, reduces interobserver variability. This is the first time that a PDT photosensitizer has been employed as a potential contrast agent; therefore, we investigated the cellular uptake patterns and extracted features at a single cell level. However, the experimental methodology and the classifier were designed to account for intensity variations that can be challenging *in vivo*. This 2-D cell culture platform served as a baseline research tool to tackle cell behavior and relevant features in organotypic models. Optimization of a 5-ALA based classification algorithm using high-density 2-D and 3-D coculture is currently under investigation. In addition, using the PDT photosensitizer provides potential selectivity in treatment due to a faster PpIX accumulation in HGD cells.<sup>36</sup> Therefore, it might be interesting to investigate the potential benefits for integrated strategies that combine detection and treatment.

## Acknowledgments

This project is supported by funding from the Natural Sciences and Engineering Research Council, Ontario graduate scholarship, Ontario Centres of Excellence, and Canadian Cancer Society (701734). S. Yeh is supported in part by the NSERC Alexander Graham Bell Canada Graduate Scholarship and Ontario Graduate Scholarship (OGS). The authors would like to thank Celine Ling and Sharon Goh for their assistance in maintaining cell culture. Q.F. holds the Canada Research Chair in Biophotonics.

## References

1. G. Portale et al., "Modern 5-year survival of resectable esophageal adenocarcinoma: single institution experience with 263 patients," *J. Am. Coll. Surg.* **202**(4), 588–96 (2006).
2. E. Sihvo, M. Luostarinen, and J. Salo, "Fate of patients with adenocarcinoma of the esophagus and the esophagogastric junction: a population-based analysis," *Am. J. Gastroenterol.* **99**(3), 419–424 (2004).
3. N. Thekkekk, S. Anandasabapathy, and R. Richards-Kortum, "Optical molecular imaging for detection of Barrett's-associated neoplasia," *World J. Gastroenterol.* **17**(1), 53–62 (2011).
4. S. J. Spechler, "The natural history of dysplasia and cancer in Barrett's esophagus," *J. Clin. Gastroenterol.* **36**(Suppl. 4), 2–5 (2003).
5. B. C. Wilson, "Detection and treatment of dysplasia in Barrett's esophagus: a pivotal challenge in translating biophotonics from bench to bedside," *J. Biomed. Opt.* **12**(5), 051401 (2007).
6. T. D. Wang and J. Van Dam, "Optical biopsy: a new frontier in endoscopic detection and diagnosis," *Clin. Gastroenterol. Hepatol.* **2**(9), 744–753 (2004).
7. M. A. Kara et al., "Characterization of tissue autofluorescence in Barrett's esophagus by confocal fluorescence microscopy," *Dis. Esophagus* **20**(2), 141–150 (2007).
8. R. Fiocca et al., "Microscopic esophagitis and Barrett's esophagus: the histology report," *Dig. Liver Dis.* **43**(Suppl. 4), S319–330 (2011).
9. J. R. Goldblum, "Barrett's esophagus and Barrett's-related dysplasia," *Mod. Pathol.* **16**(4), 316–324 (2003).
10. T. J. Muldoon et al., "Evaluation of quantitative image analysis criteria for the high-resolution microendoscopic detection of neoplasia in Barrett's esophagus," *J. Biomed. Opt.* **15**(2), 026027 (2010).
11. N. Thekkekk et al., "Pre-clinical evaluation of fluorescent deoxyglucose as a topical contrast agent for the detection of Barrett's-associated neoplasia during confocal imaging," *Technol. Cancer Res. Treat.* **10**(5), 431–441 (2011).
12. M. I. Canto, "Endomicroscopy of Barrett's esophagus," *Gastroenterol. Clin. North Am.* **39**(4), 759–769 (2010).
13. M. B. Wallace et al., "Preliminary accuracy and interobserver agreement for the detection of intraepithelial neoplasia in Barrett's esophagus with probe-based confocal laser endomicroscopy," *Gastrointest. Endosc.* **72**(1), 19–24 (2010).
14. H. Tahara et al., "Endoscopic screening of early esophageal cancer with the lugol dye method in patients with head and neck cancers," *Cancer* **66**(10), 2068–2071 (1990).
15. Y. Amano et al., "Crystal violet chromoendoscopy with mucosal pit pattern diagnosis is useful for surveillance of short-segment Barrett's esophagus," *Am. J. Gastroenterol.* **100**(1), 21–26 (2005).
16. L. M. W. K. Song et al., "Chromoendoscopy," *Gastrointest. Endosc.* **66**(10), 639–649 (2007).
17. M. I. Canto, "Staining in gastrointestinal endoscopy: the basics," *Endoscopy* **31**(6), 479–486 (1999).
18. R. Kiesslich et al., "In vivo histology of Barrett's esophagus and associated neoplasia by confocal laser endomicroscopy," *Clin. Gastroenterol. Hepatol.* **4**(8), 979–987 (2006).
19. S.-C. A. Yeh et al., "Monitoring photosensitizer uptake using two photon fluorescence lifetime imaging microscopy," *Theranostics* **2**(9), 817–826 (2012).
20. C. J. Kelty, S. L. Marcus, and R. Ackroyd, "Photodynamic therapy for Barrett's esophagus: a review," *Dis. Esophagus* **15**(2), 137–144 (2002).

21. C. J. Kelty et al., "The use of 5-aminolaevulinic acid as a photosensitizer in photodynamic therapy and photodiagnosis," *Photochem. Photobiol. Sci.* **1**(3), 158–168 (2002).
22. M. C. A. Palanca-Wessels et al., "Extended lifespan of Barrett's esophagus epithelium transduced with the human telomerase catalytic subunit: a useful in vitro model," *Carcinogenesis* **24**(7), 1183–1190 (2003).
23. L. M. F. Merlo et al., "An in vitro co-culture model of esophageal cells identifies ascorbic acid as a modulator of cell competition," *BMC Cancer* **11**(461), 1–10 (2011).
24. R. E. Kosoff et al., "Development and characterization of an organotypic model of Barrett's esophagus," *J. Cell. Physiol.* **227**(6), 2654–2659 (2012).
25. M. C. A. Palanca-Wessels et al., "Genetic analysis of long-term Barrett's esophagus epithelial cultures exhibiting cytogenetic and ploidy abnormalities," *Gastroenterology* **114**(2), 295–304 (1998).
26. Y. Su et al., "Phenotype of columnar-lined esophagus in rats with esophago-gastroduodenal anastomosis: similarity to human Barrett's esophagus," *Lab. Invest.* **84**(6), 753–765 (2004).
27. R. C. Gonzalez and R. E. Woods, *Digital Imaging Processing*, 3rd ed., Chapter 11, pp. 795–860, Prentice Hall, New Jersey (2008).
28. G. B. F. Argenti and L. Alparone, "Fast algorithms for texture analysis using co-occurrence matrices," *IEEE Proc. Radar Signal Process.* **137**(6), 443–448 (1990).
29. P. Pudil, J. Novovicova, and J. Kittler, "Floating search methods in feature selection," *Pattern Recognit. Lett.* **15**, 1119–1125 (1994).
30. R. Kohavi, "A study of cross-validation and bootstrap for accuracy estimation and model selection," in *Proc. International Joint Conference on Artificial Intelligence*, Vol. 14, pp.1137–1145 (1995).
31. C. Hsu, C. Chang, and C. Lin, "A practical guide to support vector classification," 2003, <http://www.csie.ntu.edu.tw/~cjlin/papers/guide/guide.pdf> (25 February 2015).
32. R. Ackroyd et al., "5-aminolevulinic acid photosensitization of dysplastic Barrett's esophagus: a pharmacokinetic study," *Photochem. Photobiol.* **70**(4), 656–662 (1999).
33. E. Endlicher et al., "Endoscopic fluorescence detection of low and high grade dysplasia in Barrett's oesophagus using systemic or local 5-aminolaevulinic acid sensitisation," *Gut* **48**(3), 314–319 (2001).
34. R. Bonnett, "Photosensitizers of the porphyrin and phthalocyanine series for photodynamic therapy," *Chem. Soc. Rev.* **24**, 19–33 (1995).
35. J. L. Sandell and T. C. Zhu, "A review of in-vivo optical properties of human tissues and its impact on PDT," *J. Biophotonics* **4**(11, 12), 773–787 (2011).
36. S.-C. A. Yeh et al., "5-aminolevulinic acid for quantitative seek-and-treat of high-grade dysplasia in Barrett's Esophagus cellular models," *J. Biomed. Opt.* **20**(2), 028002 (2015).

**Shu-Chi Allison Yeh** received her BSc degree in physiotherapy from Chung Shan Medical University in Taiwan in 2007 and completed her PhD degree in biomedical engineering from McMaster University, Hamilton, ON, Canada, in 2015. Her research interests include applications of steady-state and time-resolved fluorescence microscopy, and intravital imaging for diagnosis and treatment of cancer.

**Samir Sahli** received his BSc degree in applied mathematics from the University of Nice Sophia-Antipolis, France, in 2004 and his MSc and PhD degrees in physics from Laval University, Quebec, Canada, in 2008 and 2013, respectively. He joined McMaster Biophotonics Laboratory in 2013 as a postdoctoral research fellow. During his graduate studies, he has worked with Defence Research and Development Canada (DRDC-Valcartier) on the automatic detection of targets in aerial imagery. His current research interests include the development of a novel generation of gastrointestinal tract imaging device, hyperspectral imaging, image processing, and multiphoton microscopy.

**David W. Andrews** is director and senior scientist of biological sciences, Sunnybrook Research Institute. His research interests include cancer research, regulation of apoptosis by Bcl-2 family proteins, high content screening, and the development of new fluorescence microscopes to measure protein–protein interactions in live cells. He is an active member of journal editorial boards, consults in the private sector, and is on several scientific advisory boards, holds licensed patents, and has participated in several start-up companies

**Michael S. Patterson** received his BSc degree in physics from Queen's University in 1973 and his MSc degree in applied nuclear physics from McMaster University in 1976. After working for 4 years as a medical physicist, he returned to graduate school and received his PhD degree in medical biophysics from the University of Toronto for his research in ultrasonic imaging. Since joining the Juravinski Cancer Centre and McMaster in 1984, his research has focused on optical methods for diagnosis and treatment of cancer

**Qiyin Fang** is an associate professor of engineering physics at McMaster University and holds the Canada Research Chair in biophotonics. He is a member of the McMaster School of Biomedical Engineering. His current research interests include steady-state and time-resolved fluorescence spectroscopy/imaging for biomedical applications, e.g., optical biopsy, wide-field imaging, endoscopy, and microscopy. He obtained his master's and doctoral degrees from East Carolina University and his undergraduate degree from Nankai University

Biographies of the other authors are not available.